



Momentum Enhancement during Kinetic Impacts in the Low-intermediate-strength Regime: Benchmarking and Validation of Impact Shock Physics Codes

Robert Luther¹ , Sabina D. Raducan² , Christoph Burger³ , Kai Wünnemann^{1,4} , Martin Jutzi² , Christoph M. Schäfer³ , Detlef Koschny^{5,6} , Thomas M. Davison⁷ , Gareth S. Collins⁷ , Yun Zhang^{8,9} , and Patrick Michel⁸

¹ Museum für Naturkunde—Leibniz Institute for Evolution and Biodiversity Science, Berlin, Germany; robert.luther@mfn.berlin

² Space Research and Planetary Sciences, University of Bern, Switzerland

³ Institut für Astronomie und Astrophysik, University of Tübingen, Germany

⁴ Freie Universität Berlin, Germany

⁵ European Space Agency, ESTEC, Netherlands

⁶ Chair of Astronautics, TUM, Garching, Germany

⁷ Department of Earth Science and Engineering, Imperial College London, UK

⁸ Université Côte d'Azur, Observatoire de la Côte d'Azur, Laboratoire Lagrange, Nice, France

⁹ Department of Aerospace Engineering, University of Maryland, College Park, USA

Received 2022 March 15; revised 2022 August 16; accepted 2022 August 18; published 2022 October 12

Abstract

In 2022 September, the DART spacecraft (NASA's contribution to the Asteroid Impact & Deflection Assessment (AIDA) collaboration) will impact the asteroid Dimorphos, the secondary in the Didymos system. The crater formation and material ejection will affect the orbital period. In 2027, Hera (ESA's contribution to AIDA) will investigate the system, observe the crater caused by DART, and characterize Dimorphos. Before Hera's arrival, the target properties will not be well-constrained. The relationships between observed orbital change and specific target properties are not unique, but Hera's observations will add additional constraints for the analysis of the impact event, which will narrow the range of feasible target properties. In this study, we use three different shock physics codes to simulate momentum transfer from impactor to target and investigate the agreement between the results from the codes for well-defined target materials. In contrast to previous studies, care is taken to use consistent crushing behavior (e.g., distension as a function of pressure) for a given porosity for all codes. First, we validate the codes against impact experiments into a regolith simulant. Second, we benchmark the codes at the DART impact scale for a range of target material parameters (10%–50% porosity, 1.4–100 kPa cohesion). Aligning the crushing behavior improves the consistency of the derived momentum enhancement between the three codes to within $\pm 5\%$ for most materials used. Based on the derived mass–velocity distributions from all three codes, we derive scaling parameters that can be used for studies of the ejecta curtain.

Unified Astronomy Thesaurus concepts: [Impact phenomena \(779\)](#); [Asteroids \(7\)](#); [Near-Earth objects \(1092\)](#); [Asteroid satellites \(2207\)](#); [Planetary science \(1255\)](#)

1. Introduction

NASA's Double Asteroid Redirection Test (DART) will impact the secondary of the 65803 Didymos system, Dimorphos, on 2022 September 26th. The impact will cause a measurable change in the mutual orbital period within the binary system (Cheng et al. 2018; Rivkin et al. 2021, this issue). The change in orbital period is a result of the momentum imparted from the spacecraft to Dimorphos, which is enhanced by the momentum of escaping ejected material. The ejecta momentum depends on the internal structure and the target properties of Dimorphos, which are not well-constrained (e.g., Raducan et al. 2020). Formation mechanisms of double asteroids offer a large range of possible structures and material properties for Dimorphos: from a loose rubble pile agglomerate to a monolithic boulder (e.g., Zhang et al. 2021). On the one hand, the wide range of possible target properties translates to a wide range of possible orbital changes from the DART impact. On the other hand, very similar orbital changes can occur for considerably different target properties because target effects are nonunique (Raducan et al. 2020; Stickle et al. 2022, this issue). Even though DART is accompanied by

the LICIACube (Dotto et al. 2021), which is planned to observe the forming ejecta plume, more constraints on the crater and the properties of Dimorphos are needed in order to fully characterize the large-scale DART impact experiment, and to understand the kinetic impactor technique for planetary defense. Fortunately, ESA's Hera mission will arrive at the Didymos system after the DART impact in 2027 for six months of investigation. Hera will characterize the binary system in detail, in particular the physical and compositional properties of Dimorphos, including a survey of its subsurface and internal structure with a low-frequency radar on board one of the two associated Cubesats, in addition to observing the crater produced by DART (Michel et al. 2022, this issue). Most of the modeling activities in support of the development and data interpretation of Hera are supported by a consortium called NEO-MAPP (Near-Earth Object Modeling and Payload for Protection) funded by the Horizon 2020 program of the European Commission (2020–2023). The main objective of NEO-MAPP is to offer significant advances both in terms of the understanding of the response of asteroids to external forces (in particular, a kinetic impact or tidal forces during planetary approaches) and in terms of measurements by a spacecraft (including those necessary to characterize the physical and dynamical properties of the asteroid). The study presented here is part of the NEO-MAPP impact modeling activities in support of the preparation of Hera.

The change of the orbital period of Dimorphos around Didymos is a result of momentum transfer, the efficiency of which is typically expressed by the momentum enhancement factor β . This parameter represents the ratio of the change in asteroid momentum Δp_{Ast} to the impactor momentum p_{Imp} . A value of one corresponds to the transmission of the (full) impactor momentum p_{Imp} without any enhancement by ejecta; values larger than one indicate an increasing contribution from the ejecta momentum p_{ej} . The general definition of β is given by Rivkin et al. (2021, this issue), but here we focus on the simplified equation for the impact direction antiparallel to the surface normal at the impact point, neglecting any asymmetry in the ejecta plume:

$$\beta = 1 + \frac{p_{\text{ej}}}{p_{\text{Imp}}} = \frac{\Delta p_{\text{Ast}}}{p_{\text{Imp}}} \approx \frac{m_{\text{Ast}} \Delta v_{\text{Ast}}}{m_{\text{Imp}} v_{\text{Imp}}}, \quad (1)$$

with the impactor and asteroid masses m_{Imp} and m_{Ast} , respectively, the relative impact velocity v_{Imp} , and the change in the asteroid’s orbital velocity Δv_{Ast} . Predictions for β based on simulations using shock physics codes are summarized by Stickle et al. (2022, this focus issue, and references therein) and range from unity to as large as eight for target cohesions ranging from several hundred MPa down to a few Pa. Even though this variation in β depends on the variation of the target properties over a large range, a residual uncertainty—once the target properties are better constrained—is mostly due to variations in the results produced by the shock physics codes applied in the different studies.

Different shock physics codes use different numerical approaches and somewhat different material models, and they each come with a set of numerical stability parameters. These numerical details can cause noticeable variations in results. Validation studies, where numerical results are compared to laboratory experiments, or benchmark studies, where numerical simulation results are compared against each other, can be used to quantify such variations. Previous benchmark studies for shock physics codes include the Pierazzo et al. (2008) and Stickle et al. (2020) studies. Pierazzo et al. (2008) benchmarked eight different shock physics codes against each other by comparing their predictions of shock wave decay and crater growth for several idealized impact scenarios. By validating the codes’ predictions of crater growth against the results of two laboratory impact experiments (i.e., a 2 mm glass sphere impacting water (strengthless target) at 4.64 km s⁻¹, and a 6.35 mm aluminum sphere impacting an aluminum cylinder at 7 km s⁻¹), their study confirmed some variability in simulation outcomes due to the underlying solution algorithms, artificial stability parameters, material models, and spatial resolution, as well as due to choices made by individual users. They found that the general agreement between codes for overall results was within 15%–20%. Simulation results for crater size were within 10% of experimental results. Similar results have been found by Stickle et al. (2020), who conducted a benchmark study for five different codes and also directly compared their predictions of momentum enhancement caused by the simulated impacts. They varied the target strength, ranging from strengthless materials to complex rheologies, including fragmentation (damage) models. They concluded that the choice of strength model is more important than the variations between codes themselves. For similar strength models, they find variations in β of about 20%. When porosity is also considered, the scatter between the results from

different codes increases. For porosities expected to be relevant for DART (e.g., 20%), they find a variation in predicted β of 15%–30% for a basalt sphere as target, but also much larger variations by a factor of ~ 2.3 for planar targets (based on comparison of only two of the codes, CTH-3D and Spheral). Similar variations of β ($\sim 10\%$ – 30%) for a given porosity and strength have been found for comparisons of the results from different codes within the Hera Impact Working Group (e.g., Luther et al. 2019).

In this study, we further validate and benchmark three shock physics codes used within the Hera Impact Working Group. In contrast to previous work, we carefully align material models as closely as possible, in terms of the strength model and in particular the target material crushing behavior, for three shock physics codes, namely iSALE-2D, Bern SPH, and miluphcuda. First, we validate these shock physics codes against recent results of experimentally determined momentum enhancement factors (Chourey et al. 2020). Second, we model a collision akin to the DART impact on Dimorphos and benchmark the codes for a systematic range of target cohesions (between 1.4 and 100 kPa) and porosities (10% and 50%). We focus on the low-intermediate strength values. While 1.4–100 kPa is much lower than used in most of the recent DART impact studies (Stickle et al. 2022), the impacts are still in the strength regime (the transition is at around 1 Pa; see, e.g., Stickle et al. 2022). Gravity regime DART impacts, on the other hand, lead to global target deformations (Raducan & Jutzi 2022). Our results serve to quantify variation between codes for closely aligned material models, but also help to constrain the outcome of the DART impact for the given range of material properties. In addition, we derive scaling parameters based on our results, which can be used for subsequent analytical studies.

2. Shock Physics Codes and Material Description

2.1. Shock Physics Codes

All three codes applied in this study solve similar forms of the governing equations of mass, momentum, and energy conservation. However, they employ different numerical schemes: iSALE-2D uses an Eulerian grid-based approach, while miluphcuda and Bern SPH use the Lagrangian, grid-free smooth particle hydrodynamics (SPH). In SPH, each particle represents the local volume in 3D space. Individual SPH “particles” discretize the simulated materials, but are rather numerical interpolation points, instead of directly representing physical particles. In the following, we introduce each code and give some background information.

The iSALE-2D code (Wünnemann et al. 2006) is based on the SALE hydrocode solution algorithm (Amsden et al. 1980). It is a grid-based ALE (Arbitrary Lagrangian Eulerian) code and uses a finite difference scheme. The package includes different material models, including an elasto-plastic constitutive model, fragmentation models, various equations of state, and multiple materials (Melosh et al. 1992; Ivanov et al. 1997). More recent updates include a modified damage model with an intact and a damaged yield surface (Collins et al. 2004) and the ε - α porosity compaction model (Wünnemann et al. 2006; Collins et al. 2011). Although a 3D version of iSALE exists, we apply the 2D version in this study, which reduces computational costs. The code makes use of a cylindrical symmetry around the vertical axis along the projectile trajectory to simulate 3D behavior. As a consequence, impact angles are limited to 90°, and each cell

represents a hollow cylindrical-shaped element (torus with a rectangular cross-sectional area). To further reduce the computational efforts required for a single computation, we follow the approach described by Raducan et al. (2019) and halve the resolution in iSALE simulations several times, as indicated in the validation and benchmark sections (Sections 3 and 4). Such a regridding procedure proved to speed up calculations, while maintaining the accuracy of crater and momentum enhancement calculations (e.g., 1% deviation between a high-resolution model and a regridded model; Raducan et al. 2019).

The 3D SPH code miluphcuda (Schäfer et al. 2016, 2020) has been mainly developed for modeling astrophysical impact and collision processes of multi-material, self-gravitating bodies, and utilizes fast and efficient GPU hardware. It includes several rheology models to simulate elasto-plastic flows as well as brittle failure, various equations of state, and different porosity compaction models like the P- α model. In previous works, miluphcuda has been successfully used for simulations of granular media (e.g., Schäfer et al. 2017) and porous materials (e.g., Haghighipour et al. 2018; Grishin et al. 2020).

Bern's SPH code was originally developed by Benz & Asphaug (1995, 1994) to model the collisional fragmentation of rocky bodies. This code was parallelized (Nyffeler 2004) and further extended by Jutzi et al. (2013, 2008) and Jutzi (2015) to model porous and granular materials. The most recent version of the code includes a tensile fracture model (Benz & Asphaug 1994, 1995), a porosity model based on the P- α model (Jutzi et al. 2008, 2009), pressure-dependent strength models (Jutzi 2015), and self-gravity. Like miluphcuda, this is a 3D code.

2.2. Material Models

All three codes use similar constitutive models and equations of state. In the following, we describe the details of the strength and porosity compaction models.

2.2.1. Rheology Model

In this study, we focus on impacts into granular materials, which is why we make use of a simpler strength model without including a dedicated damage (fragmentation) model. Typically, a Drucker–Prager yield surface is used for such scenarios without any damage accumulation (e.g., Elbeshhausen et al. 2009; Wünnemann et al. 2016; Prieur et al. 2017; Schäfer et al. 2017; Luther et al. 2018), which relates the yield strength Y to the pressure P as

$$Y(P) = \min(Y_0 + fP, Y_{\max}), \quad (2)$$

with the cohesion Y_0 , the coefficient of friction f , and the limiting strength at the Hugoniot elastic limit Y_{\max} (Figure 1). The choice of parameters is derived from Chourey et al. (2020), who provide the Mohr–Coulomb angle of internal friction ϑ_f^{MC} for regolith simulants (the experiment is explained further below in Section 3.1). The Mohr–Coulomb angle needs to be translated into a Drucker–Prager coefficient of friction, which is not trivial. In principal stress space, the Coulomb yield surface has a hexagonal cross section, while the Drucker–Prager yield surface has a circular cross section. Different expressions relate the coefficients of friction between the two models, depending on whether the circle inscribes or circumscribes the hexagon, (e.g., Davis & Selvadurai 2005). While the expression used by, e.g., Elbeshhausen et al. (2009) yields coefficients of friction for a circle

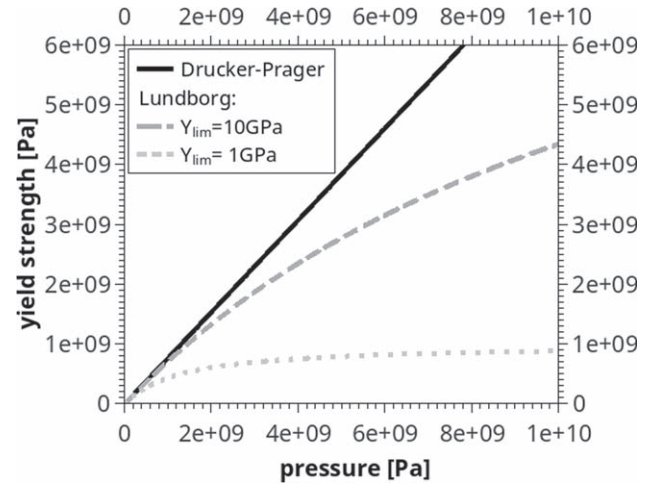


Figure 1. Yield surfaces: Drucker–Prager & Lundborg with limiting strengths of 1 GPa and 10 GPa, 1.4 kPa cohesion, and a coefficient of friction of 0.77. The Lundborg curves asymptote to the limiting strength.

inscribing the Mohr–Coulomb yield surface, here we use an expression that yields coefficients close to the average results between minimum and maximum coefficient:

$$f^{DP} = \frac{2\sqrt{2} \sin \vartheta_f^{MC}}{3 - \sin \vartheta_f^{MC}}. \quad (3)$$

The determination of shear failure is done by comparing the second invariant of the deviatoric stress tensor to the yield envelope. Once it exceeds the yield strength, the material behaves plastically and the updated deviatoric stress (and strain) components are reduced to the yield envelope (Collins et al. 2004). In addition, in iSALE and Bern SPH, negative pressures are capped by the intersection of the yield envelope with the pressure axis, which is at some $p < 0$ for nonzero cohesion. In miluphcuda, the yield strength curve always follows a slope = 1 for $p < 0$, hence negative pressures are always capped at $-Y_0$. This is intended to eliminate a potentially unphysical influence of the friction coefficient (the slope of the yield strength curve for $p > 0$) on the negative pressure cap for low coefficients of friction. In all models, the minimum allowed pressure is zero if the cohesion is set to zero.

A weakness of the Drucker–Prager strength model is that it shows an abrupt change in dY/dP at high pressure. In contrast, the Lundborg parameterization (Lundborg 1968) asymptotes to a maximum pressure, while at low pressures it is approximately equivalent to the Drucker–Prager model. Hence, we use the Lundborg yield surface for all simulations. For the validation simulations, the Hugoniot elastic limit is set to 10 GPa in order to align with the Drucker–Prager curve at pressure sufficiently below 10 GPa (Figure 1). This value appears unrealistically high, but has little influence on the material response at relatively low velocities (i.e., low peak pressures). However, for our benchmark simulations of DART-like impacts at 6–7 km s⁻¹, we reduce the limit to a more realistic value of 1 GPa. The Lundborg yield surface is expressed as

$$Y(P) = Y_0 + \frac{fP}{1 + \frac{fP}{Y_{\max} - Y_0}}. \quad (4)$$

All three codes include weakening mechanisms for special conditions like low-density states, where material strength is typically reduced. For iSALE, we follow previous studies and apply a low-density weakening for cells with a density below 0.85 times the reference density (see Appendix for details).

In Bern SPH, we apply a strain-based weakening model, in which cohesion is reduced with increasing total strain ε_{tot} . For $\varepsilon_{\text{tot}} \geq 1$ cohesion is lost (see Appendix).

In miluphcuda, we apply a smooth strength weakening for states below the reference density, based on reduction of the cohesion, which in turn reduces the entire yield envelope. Refer to the Appendix for details.

2.2.2. Porosity Compaction Model

In this section, we discuss the parameterizations used to simulate the compaction of pore space. The porosity models in all three codes do not resolve grains or microscopic pore space. Instead, a macroscopic parameterization is used to describe the microscopic material behavior. The iSALE-2D simulations utilize the ε - α compaction model (Wünnemann et al. 2006; Collins et al. 2011), which relates the distension, α , to the volumetric strain, ε . The two SPH codes use the so-called P - α compaction model (Jutzi et al. 2008, 2009), which is based on a relation between distension, α , and pressure, P . As the codes apply different porosity models, for the validation and benchmark scenarios described in this paper, we align the crushing behavior (e.g., distension as a function of pressure) used in each of the models (see Sections 3 and 4, respectively). Here, we include a brief description for each porosity model.

The ε - α compaction model describes four different compaction regimes: (i) elastic compaction, (ii) exponential compaction, (iii) power-law compaction, and (iv) complete compaction, and in our description, we focus on the second and third regimes. For further details and applications, we refer to Wünnemann et al. (2006) and Collins et al. (2011). Note that the volumetric strain ε is negative in compression. Also note that iSALE internally uses the compaction rates $d\alpha/d\varepsilon$, which can be derived from the following equations.

In the exponential compaction regime, which applies for strains smaller (more negative, i.e., larger in absolute number) than the volumetric strain at the elastic limit ε_e (and the corresponding distension α_e , which is computed by the model), the distension behaves as

$$\alpha(\varepsilon) = \alpha_e e^{\kappa(\varepsilon - \varepsilon_e)}, \quad (5)$$

with the compaction rate parameter κ , which typically is set to a value between 0.8 and 1, depending on the initial porosity. When the distension decreases below the transition value α_x (with corresponding transition volumetric strain ε_x), the compaction model transitions into the power-law regime and distension decreases according to¹⁰

$$\alpha(\varepsilon) = 1 + (\alpha_x - 1) \left(\frac{\varepsilon_c - \varepsilon}{\varepsilon_c - \varepsilon_x} \right)^2, \quad (6)$$

until full compaction, i.e., $\alpha = 1$ (with corresponding compaction volumetric strain ε_c , which is derived by the continuity condition between power law and exponential regime; see Wünnemann et al. 2006, for details). The ε - α compaction

model has been successfully applied and validated by comparing the macroscopic behavior to mesoscale models, where grains or pores were directly resolved, and by comparison to laboratory experiments or observations (Güldemeister et al. 2013; Kowitz et al. 2013; Davison et al. 2016; Luther et al. 2017).

In contrast to the ε - α compaction model, the P - α compaction model defines distension as a function of pressure P . The model applies a function defined by the parameters P_e , P_s , P_t , n_1 , n_2 , α_t and the initial distension, α_0 (Jutzi et al. 2008). There are two compaction regimes with different power-law slopes n_1 , n_2 , separated by the transition pressure $P_e < P_t \leq P_s$ and distention $1 \leq \alpha_t < \alpha_0$. This model has been successfully applied and validated by reproducing laboratory crush curve measurements and impact disruption experiments (e.g., Jutzi et al. 2009; Jutzi 2015). To match the crush curves in the two porosity models, we use a simplified version of the P - α compaction model, with a single power-law slope (the transition distension $\alpha_t = 1$ also corresponds to the final distension). As a result, $P_s = P_t$ and the model reduces to

$$\alpha(P) = 1 + (\alpha_e - 1) \left(\frac{P_s - P}{P_s - P_e} \right)^{n_1} \quad (7)$$

3. Validation against Experimental Impacts into Regolith Simulant

In this section, we validate the three codes, iSALE-2D, Bern SPH, and miluphcuda, against impact experiments into regolith simulant performed by Chourey et al. (2020), which are briefly summarized in the next section.

3.1. Laboratory Experiments into Regolith Simulant

We chose a validation scenario of impact experiments conducted in a material that is likely similar to an asteroid environment, and which, as such, applies to the kinetic impactor technique. We limited our choice to experiments with homogeneous target materials, due to their compatibility with our material models. The experiments were conducted at hypervelocity speeds for the given target material and recorded measurements of the momentum enhancement (Chourey et al. 2020).

Chourey et al. (2020) have conducted 57 impact experiments into glass bead, quartz sand, and regolith simulant targets, using an electrostatic accelerator and a cylindrical PVC projectile (for details, we refer to their publication). Impact velocities ranged from 1 to 2.5 km s⁻¹. The target material was filled into a hemispherical 20 cm diameter steel bowl, which was attached to a spring system (Figure 2(a)). The post-impact oscillations were used to determine the transferred momentum onto the target. For each experiment, 16 high-speed camera images were taken and cover about 1 ms of the crater formation process. In addition, the final rim-to-rim diameters and the angles of the ejecta curtain were measured. In this study, we focus on the impacts into regolith simulant (numbered as #37–#48 out of the 57 experiments) as it represents the best analog to asteroid surface material.

3.2. Material Parameters Used for the Validation Setup

Chourey et al. (2020) give the Mohr–Coulomb angle of internal friction ϑ_f^{MC} for regolith simulant as 40°. According to Equation (3), this yields a coefficient of friction of ~ 0.77 . The

¹⁰ Note that the power-law regime in Equation (2) in Collins et al. (2011) includes a typo: Instead of ε_e in the denominator, it should say ε_x .

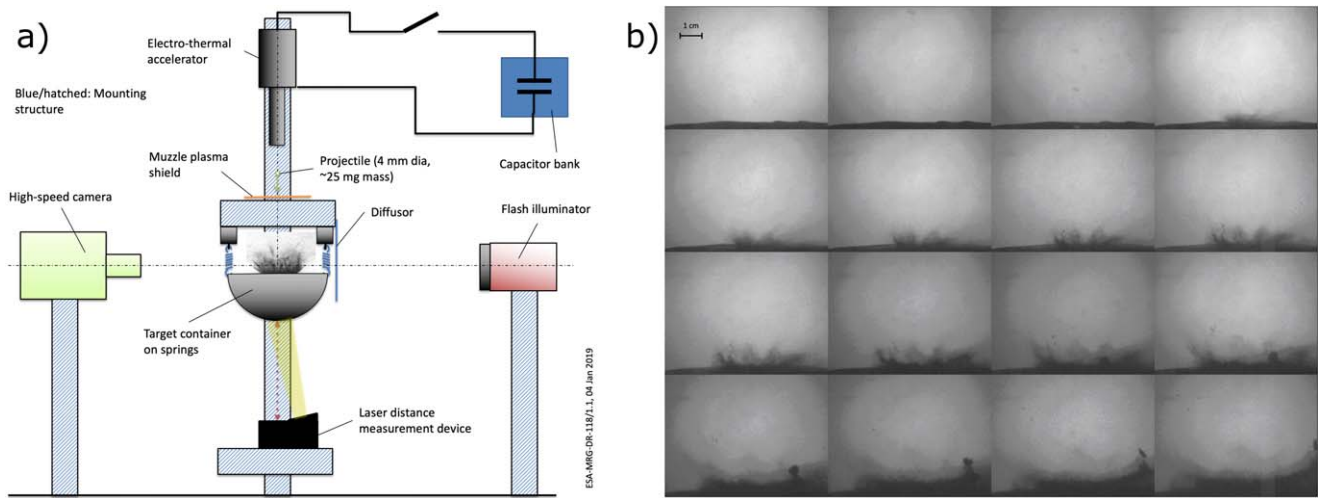


Figure 2. Experimental setup (a) and example high-speed images for regolith simulant (b) as illustrated by Chourey et al. (2020) in their Figures 2 & 10.

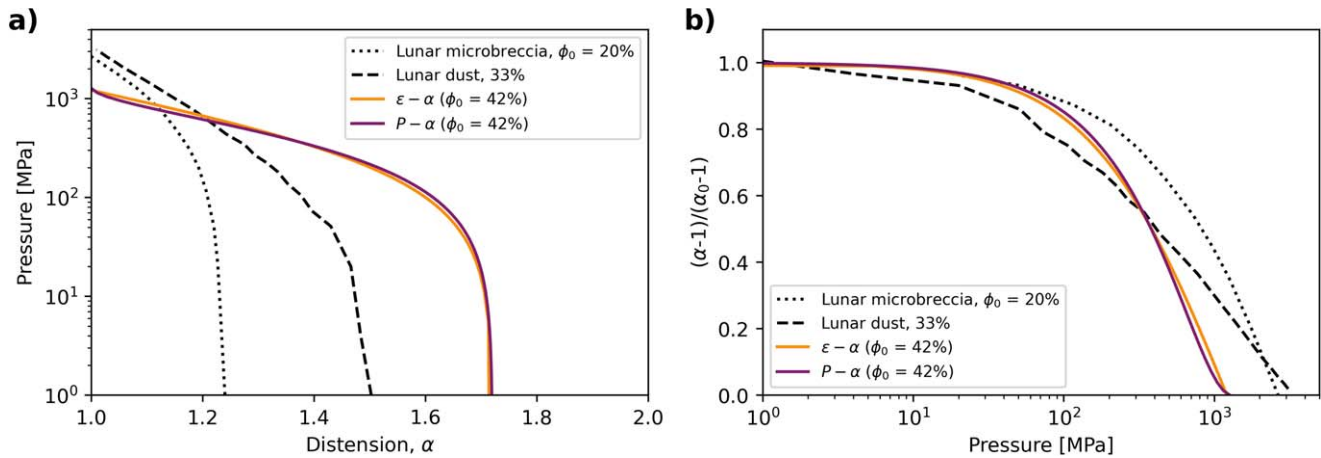


Figure 3. Crush Curves. We compare the crushing behavior for the same regolith material using two different compaction models: ϵ - α compaction model (iSALE) and P - α compaction model (both SPH codes). For comparison, we add the crush curves for lunar microbreccia and lunar dust (Stephens & Lilley 1970). The left panel shows the pressure–distension relation, and the right panel shows the same for a normalized distension.

Table 1
Porosity Parameters for Regolith Simulant (Initial Porosity $\Phi = 42\%$ /Initial Distension $\alpha_0 = 1.72$)

iSALE-2D/ ϵ - α compaction model			
Elastic Volumetric threshold ϵ_e	Transition distension αx	Compaction efficiency κ	Sound speed ratio χ
-2.0D-08	1.1	0.96	0.3
SPH/ P - α compaction model			
Elastic pressure P_e [Pa]	Solid pressure P_S [GPa]	n_1 , initial compaction	
100.0	1.3	2.0	

regolith simulant shows a cohesion of ~ 1.4 kPa (Chourey et al. 2020). The porosity of the regolith simulant used in the experiments from Chourey et al. (2020) depends on the compaction during target preparation and ranges from $\sim 33\%$ to 42% . The corresponding densities are 1913 kg m^{-3} – 1660 kg m^{-3} , respectively, while the grain density is 2905.8 kg m^{-3} . As discussed in Section 2.2.2, we align the compaction behavior for the codes: For the chosen set of porosity parameters (Table 1), the three codes give similar crush curves (Figure 3).

In all three codes, the thermodynamical behavior of the PVC projectile and the regolith simulant target are modeled by

simple Mie–Grüneisen and Tillotson equations of state, respectively (see Table A2 in the Appendix for details).

To reduce computational costs in iSALE simulations, we halve the resolution once during the simulation, starting with 20 cells per projectile radius (CPPR), and ending with 10 CPPR. Our initial high-resolution zone consisted of 700 horizontal and 560 vertical cells. Further model parameters are listed in Table A1 in the Appendix.

The miluphcuda simulations comprise roughly 800k SPH particles. The resolution (particle density/spacing) in the flat, half-sphere target decreases radially from the impact point to optimize accuracy. The spherical projectile’s particle

Table 2
Model Results in Regolith Simulant for iSALE-2D, Bern SPH, and Miluphcuda

No.	m_{Pr} (mg)	v_{Pr} (km s ⁻¹)	Laboratory			iSALE		Bern SPH		miluphcuda	
			D_{rim} (cm)	D_{surf} (cm)	β						
#40	24	2.00	5.2	4.52	1.38	3.92	1.36	4.40	1.37
#41	24	1.43	5.3	4.61	1.25	3.36	1.27	3.34	1.32	4.10	1.32
#42	24	2.22	5.3	4.61	1.28	4.08	1.38	3.80	1.35	4.80	1.40
#46	25	2.50	5.8	5.04	1.37	4.42	1.42	3.90	1.36	5.60	1.43

Note. The columns show projectile mass m_{Pr} and velocity v_{Pr} , experimental crater diameters at rim level D_{rim} , an estimate for the crater diameter at pre-impact surface level D_{surf} ($D_{surf} = D_{rim} / 1.15$), and the momentum enhancement factor β .

number is chosen to closely match the resolution at the target center. This results in the projectile diameter being resolved by approximately eight SPH particles.

The models for Bern SPH were run with 3.5 million SPH particles. The projectile was made up by 75 particles.

3.3. Validation Results

The simulation results from our models are summarized together with the experimental results for the shots with velocities between 1.43 km s⁻¹ and 2.5 km s⁻¹ in Table 2 and are shown in Figure 4. To compare experimentally derived rim-to-rim diameters with the pre-impact surface diameters of the simulations, the experimental values were translated into pre-impact surface level diameters as $D_{surf} = D_{rim} / 1.15$. The factor of 1.15 is slightly smaller than the factor of 1.3 given by Housen & Holsapple (2011) for less cohesive materials, but agrees with iSALE simulations. We mark the uncertainty from this translation by plotting the upper and lower end of the uncertainty according to factors of 1.3 and 1.0, respectively (Figure 4(a)).

For the crater diameters at pre-impact surface level, we generally find similar results for all three codes, where the variation among the codes is comparable to those in the experimental results (Table 2 and Figure 4(a)). For the fastest impact (#46; see Table 2), the deviations of the individual codes from the average reach up to 20%, but fall below 15% for the remaining scenarios.

The validation results for the momentum enhancement factor β are shown in Figure 4(b). All three codes provide results that are in close agreement with each other, and with the experimental results, which show more scatter than the numerical results. Even though the results for crater sizes show a deviation of up to 20%, the results for the momentum enhancement all lie within $\pm 3\%$.

3.4. Discussion of the Validation

The simulated crater diameters are in close agreement with the experimental craters for most of the simulated cases. For an impact velocity of 2.5 km s⁻¹, the discrepancies between all models are the largest and spread as much as the uncertainty range from the experiment. For this velocity, results from Bern SPH are slightly smaller than the experimental craters. In general, the diameters derived with iSALE and Bern SPH are in closer agreement with each other, but nevertheless, the results from miluphcuda fall always within the given uncertainty. All three codes yield momentum enhancement factors in very close overlap with each other, within about $\pm 1\%$ from the average. They are mostly close to the experimental results, and much closer to each other than the scatter of the experimental

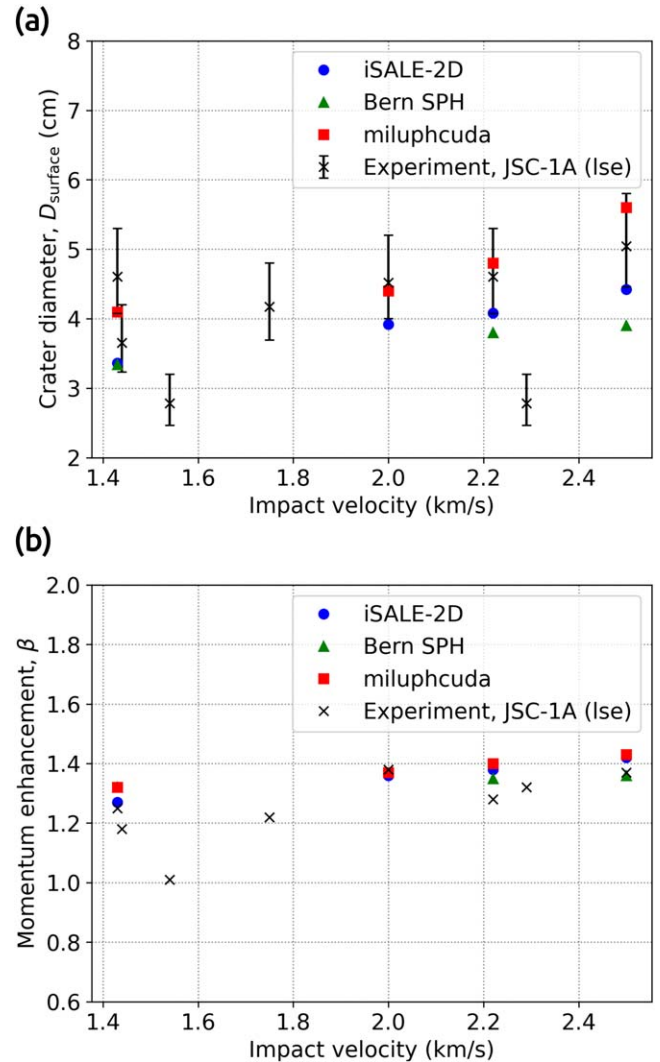


Figure 4. Validation results for iSALE, Bern SPH, and miluphcuda in regolith simulant targets. The top panel (a) shows results for surface crater diameters, the bottom panel (b) for β . The data are listed in Table 2. The error bars in the top panel do not refer to experimental uncertainties; instead, they estimate the uncertainty in converting rim–rim diameters (as measured by Chourey et al. 2020) to pre-impact surface diameters. The upper limits of the bars correspond to a ratio of $D_{rim}/D_{surf} = 1$, while the lower limits indicate $D_{rim}/D_{surf} = 1.3$ (as stated by Housen & Holsapple 2011). For our simulations, we inferred a most probable factor of ~ 1.15 , based on our iSALE models.

data. It is important to note that the experimental results show a significant scatter, which makes it more difficult to compare the model with the experiment and is not accounted for by the given uncertainty range in Figure 4. A possible source of errors

could come from the experimental setup (e.g., the shaking of the whole system after impact).

Another source of scatter in the experimental data might come from variations in target preparation or atmospheric conditions (e.g., humidity) during the shooting campaign, which lasted about two weeks (Koschny, personal communication). Such variations could translate into small variations of the target properties (cohesion, coefficient of friction, and porosity), leading to a variation of observed crater diameters and momentum enhancement. Such a variation should affect both observables in the same way, e.g., an increase of the strength should decrease both crater size and momentum enhancement, which can be observed for #37 (at 1.54 km s^{-1} impact velocity). Hence, we excluded this shot from the model series. In contrast, #39 (at 2.29 km s^{-1}) shows a significantly smaller crater as compared to the average trend, while the momentum enhancement seems to be unaffected. Due to this uncertainty, this shot was also not modeled in the validation series. In order to test the effect of a slight change of the strength of the target, we also ran a model with a coefficient of friction of 0.64: Decreasing the coefficient of friction by ~ 0.1 increases the crater diameter and the momentum enhancement by $\sim 17\%$ (equaling 0.9 cm) and $\sim 18\%$ ($\Delta\beta = 0.24$), respectively (Figure 5). Hence, detailed characterization of the target material is important for yielding precise results. Nevertheless, we consider the validation based on the chosen material parameters as successful.

3.5. From Laboratory Scale to the DART Scale

After successful validation against the laboratory experiments from Chourey et al. (2020), we expanded the scenario to the scale of a DART-like impact for benchmarking the codes at the relevant scale. This scenario differs in three regards: (i) DART's impact speed is much larger than the impact speeds in the laboratory experiments, (ii) the experiment is conducted under Earth's gravity, while the DART impact takes place in a low-gravity environment, and (iii) DART's mass is seven orders of magnitude larger than the projectile in the experiments. Previous studies have shown that the momentum enhancement depends on such scale effects (Holsapple & Housen 2012; Housen & Holsapple 2015; Walker et al. 2013; Jutzi & Michel 2014; Walker & Chocron 2015; Durda et al. 2019; Schimmerohn et al. 2019; Chourey et al. 2020). To bridge the gap between the different regimes and study the effect on crater size and momentum enhancement, we conducted additional simulations with iSALE, where we (i) increased the velocity up to 7 km s^{-1} based on the laboratory setup, but kept the impactor mass the same as in the experiment, and (ii) decreased gravity to $5e-5 \text{ m s}^{-2}$ (Table 3 and Figure 5). These models were consistently conducted with a porosity of 33%, which corresponds to the upper density of regolith simulant (1913 kg m^{-3}) provided by Chourey et al. (2020). The crater diameter increases with increasing impact velocity (up to 6.4 cm at 7 km s^{-1}). The increase follows the expected scaling relations from Housen & Holsapple (2011) for the material-dependent scaling exponent $\mu = 0.37$ (Figure 5(a)). Details are given in the figure caption. Similarly to the crater diameter, the momentum enhancement also increases with increasing impact velocity by 0.4 from 1.4 at 2.5 km s^{-1} to 1.8 at 7 km s^{-1} (28% increase). We have fitted a power law to the increase and compared our results to the extrapolation from Chourey et al. (2020). With an exponent of

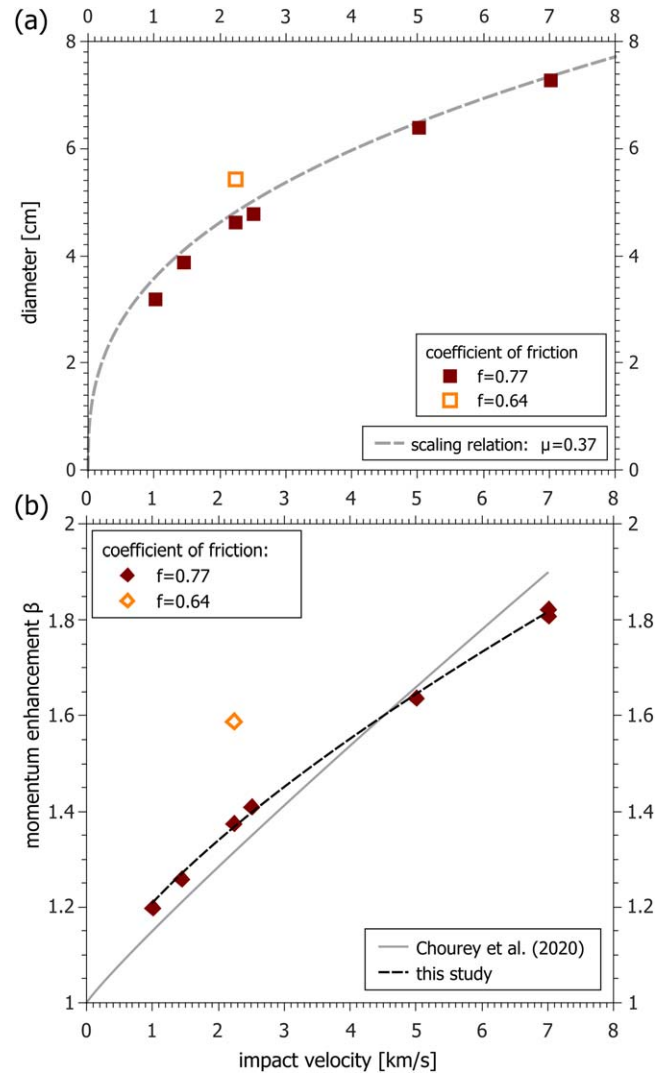


Figure 5. Rim-to-rim crater diameter (a) and momentum enhancement β (b) for increasing impact velocity for regolith simulant. The numerical results are listed in Table 3. The projectile mass was 24 mg . The experimental velocity range was extended above 2.5 km s^{-1} into the DART regime. Colors indicate a variation in the coefficient of friction. The results for crater size scaling in the strength regime (panel a) are given according to Housen & Holsapple (2011), including the densities of projectile and target, and using the scaling exponent $\nu = 0.3$. The scaling exponent $\mu = 0.37$ (dashed gray line) was derived from fitting procedures for ejection velocities as described by Luther et al. (2018). The scaling factor is $H_2 = 0.55$, and the effective strength was set to the value for the cohesion. The gray line in panel (b) shows the estimated dependence of β from the impact velocity v_{pr} from Chourey et al. (2020): $\beta = 1 + 0.15 v_{pr}^{0.92}$. The dashed black line shows our fit: $\beta = 1 + 0.21 v_{pr}^{0.7}$. The velocity exponent can be translated into the scaling exponent μ by the following relation (Holsapple & Housen 2012): $\beta \sim 1 + v_{pr}^{3\mu-1}$, which gives values of $\mu = 0.64$ and $\mu = 0.56$ for both relations, respectively.

0.7 compared to 0.92 , we find a slightly slower increase and can refine the extrapolations (Figure 5(b)). The large gravity decrease has almost no effect and can hardly be seen in Figure 5. At the DART scale, the impact is clearly strength-dominated. This is expected, as the strength-gravity regime transition is at $\sim 1 \text{ Pa}$ (Stickle et al. 2022, this issue).

4. Benchmark on the Scale of the DART Impact

Having validated the results for iSALE-2D, miluphcuda, and Bern SPH against laboratory results, we expand the

Table 3
Cratering in Regolith Simulant^a

Impact Velocity (km s ⁻¹)	1.0	1.44	2.22	2.5	5.0	7.0	7.0 ^b
Crater diameter D_{surf} (cm)	2.7	3.1	4.0	4.0	5.5	6.4	6.4
Rim crater diameter D_{rim} (cm)	3.2	3.9	4.64	4.8	6.4	7.3	7.5
Momentum enhancement	1.20	1.26	1.375	1.41	1.64	1.81	1.82

Notes.

^a Target properties: cohesion 1.4 kPa, coefficient of friction 0.77, upper density limit provided by Chourey et al. (2020) of 1913 kg m⁻³ (corresponding to $\Phi = 33\%$), 24 mg projectile mass (with initial 20 CPPR), Earth gravity, limiting strength $Y_{\text{lim}} = 1$ GPa.

^b Low-gravity environment.

Table 4
Porosity Parameters for Potential Dimorphos-like Target Materials

iSALE-2D/ ε - α Compaction Model					
Porosity Φ [%]	Initial Distension α_0	Elastic Volumetric Threshold ε_e	Transition Distension α_x	Compaction Efficiency κ	Sound Speed Ratio χ
10	1.11	-2.0D-08	1.05	0.76	0.8
20	1.25	-2.0D-08	1.05	0.88	0.6
30	1.429	-2.0D-08	1.10	0.94	0.3
40	1.667	-2.0D-08	1.10	0.96	0.3
50	2.0	-2.0D-08	1.15	0.98	0.3
SPH/ P - α Compaction model					
Porosity Φ [%]	Initial distension α_0	Elastic pressure P_e [Pa]	Solid pressure P_S [GPa]	n_1 , initial compaction	
10	1.11	100.0	1.8	1.2	
20	1.25	100.0	1.7	1.45	
42	1.72	100.0	1.3	2.0	
50	2.0	100.0	1.0	3.0	

benchmarking exercise to a full-scale DART-like scenario with a regolith target with similar characteristics to the regolith simulant in the validation experiments. For benchmarking the three codes, we consider vertical impacts with respect to a planar target at 6 km s⁻¹, of a 1 m in diameter, 600 kg, spherical aluminum projectile for a range of target properties. To reduce effects of different impactor geometries and to avoid difficulties in resolving the solar panels, we neglect the solar panels and concentrate all mass in the spacecraft bus, which can lead to a slight overestimation of the resulting momentum enhancement compared to when the full spacecraft geometry is used (Owen et al. 2022).

4.1. Material Parameters for Benchmark Simulations

We use targets with a constant coefficient of friction of 0.77 and varying cohesion ($Y_0 = 1.4, 10$ and 100 kPa) in order to cover a range of possible target properties. For those scenarios, all three codes use a Lundborg yield strength parameterization with a realistic high-pressure yield strength limit of 1 GPa. At an impact speed of 6 km s⁻¹, much more material is subject to high pressure >1 GPa and the effect of the strength limit is not negligible. The initial porosity is varied between $\Phi_0 = 10\%$ –50%, and similarly to Section 3, we carefully choose parameters for the porosity models (Table 4) that align the crush curves for each individual porosity (Figure 6).

To reduce computational costs, we halve the resolution in iSALE simulations after 3 ms, 6 ms, and 8 ms, starting with a resolution of 40 cells per projectile radius (CPPR), and ending with 5 CPPR. Our initial high-resolution zone consists of 1000

horizontal and 2400 vertical cells, and we add 500 cells to the bottom and the right side of the grid during the first regridding. Further model parameters are listed in Table A1 in the Appendix.

The miluphcuda simulations comprise roughly 500k SPH particles. The resolution (particle density/spacing) in the flat, half-sphere target decreases radially from the impact point to optimize accuracy. The spherical projectile’s particle number is chosen to closely match the resolution at the target center. This results in the projectile diameter being resolved by approximately 6 SPH particles.

The models for Bern SPH were run with five million SPH particles. The projectile was comprised of 81 particles.

4.2. Benchmark Results

Our analysis for the DART-like benchmark scenarios includes determining the ejecta mass, launch angle, and launch velocity. The ejection behavior, in terms of cumulative ejecta mass versus launch velocity, is shown in Figure 7 for 20% and 50% porosity for cohesions from 1.4 kPa to 10 kPa and 100 kPa. Comparing the general ejection behavior, we find that both SPH codes predict faster launch velocities than are observed with iSALE. Toward the slow end of the velocity distribution, we find similar total cumulative masses for all codes. As expected from previous studies (e.g., Luther et al. 2018; Raducan et al. 2019), an increase of the cohesion from 1.4 kPa to 10 kPa and 100 kPa reduces the total amount of ejected mass for all porosities, while the fastest ejection velocities remain unchanged. Similarly, increasing porosity

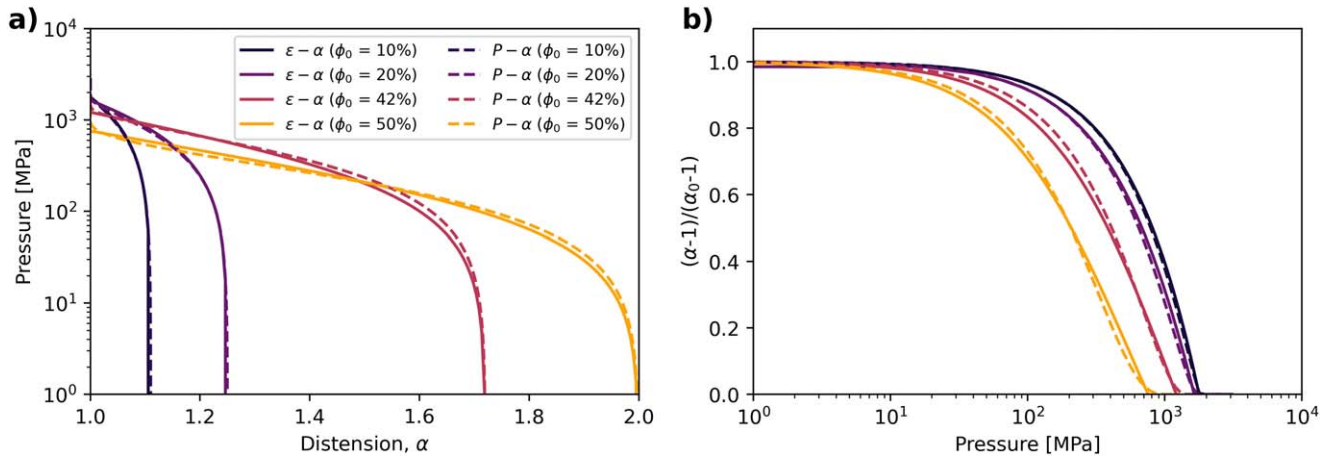


Figure 6. Crush curves for the same regolith material using two different porosity compaction models: ϵ - α (iSALE) and P - α (both SPH codes). All parameters are given in Table 4. The left panel shows the pressure–distension relation, and the right panel shows the same for a normalized distension.

also leads to a decrease in the total ejected mass, but also to a decrease of the fastest ejection velocities. This results in decreasing momentum enhancement for increasing porosity as well as for increasing cohesion (Figure 8).

In general, we find an agreement for the momentum enhancement between the two SPH codes and iSALE results of $\pm 5\%$ for 1.4 and 10 kPa cohesion (or better; Figure 8). For a cohesion of 100 kPa, the deviation is larger, but remains within a range of $\pm 10\%$ from the average value.

4.3. Discussion of the Benchmark

For benchmarking the three codes, we carefully chose similar material models and parameters. Previous studies (Luther et al. 2019; Stickle et al. 2020) found deviations for the momentum enhancement β between different codes in a range of $\pm 10\%$ – 15% . Stickle et al. (2020) showed a difference of 25% between the grid-based code CTH (3D) and the meshless code Spheral (3D) at the DART-relevant porosity of 20%. They concluded that those differences result from the different porosity models applied. Similarly, Luther et al. (2019) observed that differences in β between codes depend on the chosen crush curve (for the same porosity). For the simulations in this work, we took particular care to align the porosity compaction behavior between codes (Figure 6), which results in a considerably better agreement, within $\pm 5\%$ for most cases (Figure 8).

Target properties have an important influence on the ejecta characteristics (i.e., launch speeds and angles, and ejected mass), as well as the resulting momentum enhancement. In this study, we compare the cumulative ejecta mass–velocity distributions for various cohesion and porosity combinations, illustrated in Figure 7, and the resulting β (Figure 8). Previous studies have shown that an increase of the target’s coefficient of friction or cohesion decreases the crater size (e.g., Prieur et al. 2017), and therefore also the amount of ejected material. On the other hand, increasing friction decreases the ejection angle, and hence, also the vertical component of the velocity vector, which also reduces the vertical momentum carried away by ejecta (Luther et al. 2018; Raducan et al. 2019; see Figure 5). An increase of cohesion reduces the mass of slow ejecta, while ejection speeds and angles of the remaining ejecta are largely unmodified. Increasing porosity has only a small effect on ejection angles, but decreases the fastest ejection velocities

from ejecta originating close to the impact point, and reduces crater size and therefore also the ejected mass (Prieur et al. 2017; Luther et al. 2018). As a consequence, increasing porosity decreases the momentum enhancement as shown by Raducan et al. (2019) and Bruck Syal et al. (2016), as well as in our study. For a given (initial) porosity, the detailed definition of the crush curve influences the momentum enhancement, as it defines how easily material is compacted and how much energy is needed for pore crushing. By aligning the crush curves, we make sure that all three codes simulate the same material response, not only in terms of initial porosity, but also in terms of its compaction behavior and the energy going into crushing.

Comparing the cumulative ejecta masses over velocity for the three codes (Figure 7), we note a difference in the fastest ejecta, which has a mass of less than a few impactor masses. The ejection speed of the fastest ejecta resolved by the grid-based code iSALE is considerably slower than that obtained with the particle-based Bern SPH and (even more so) miluphcuda. The mass of the different fastest ejecta accounts for about one projectile mass or less. This difference is likely related to the principal numerical differences between the codes: Groups of particles can be ejected in SPH at the observed high velocity, while the material interface algorithm in iSALE, which is meant to suppress numerical diffusion, rather avoids the separation of material into single, under-resolved cells. The existence of these fast particles in SPH could partly explain the slightly larger values of β for SPH. Another important difference between the three codes that should be noted is that both SPH codes are 3D codes and each particle represents its own mass, while in iSALE, each cell or tracer represents a cylindrical symmetric mass (i.e., a square toroid). As a consequence, tracers from the early ejection flow in iSALE, which originate from near the impact point, represent a smaller mass than an SPH particle, while tracers that originate from a larger radial distance represent a larger mass. The total cumulative ejecta mass derived with all three codes is in close agreement.

4.4. Application of Scaling Relationships to the Benchmark Data

To quantify the agreement between the three codes, apart from the comparison of the momentum enhancement, we compare the cumulative mass plots in the light of scaling

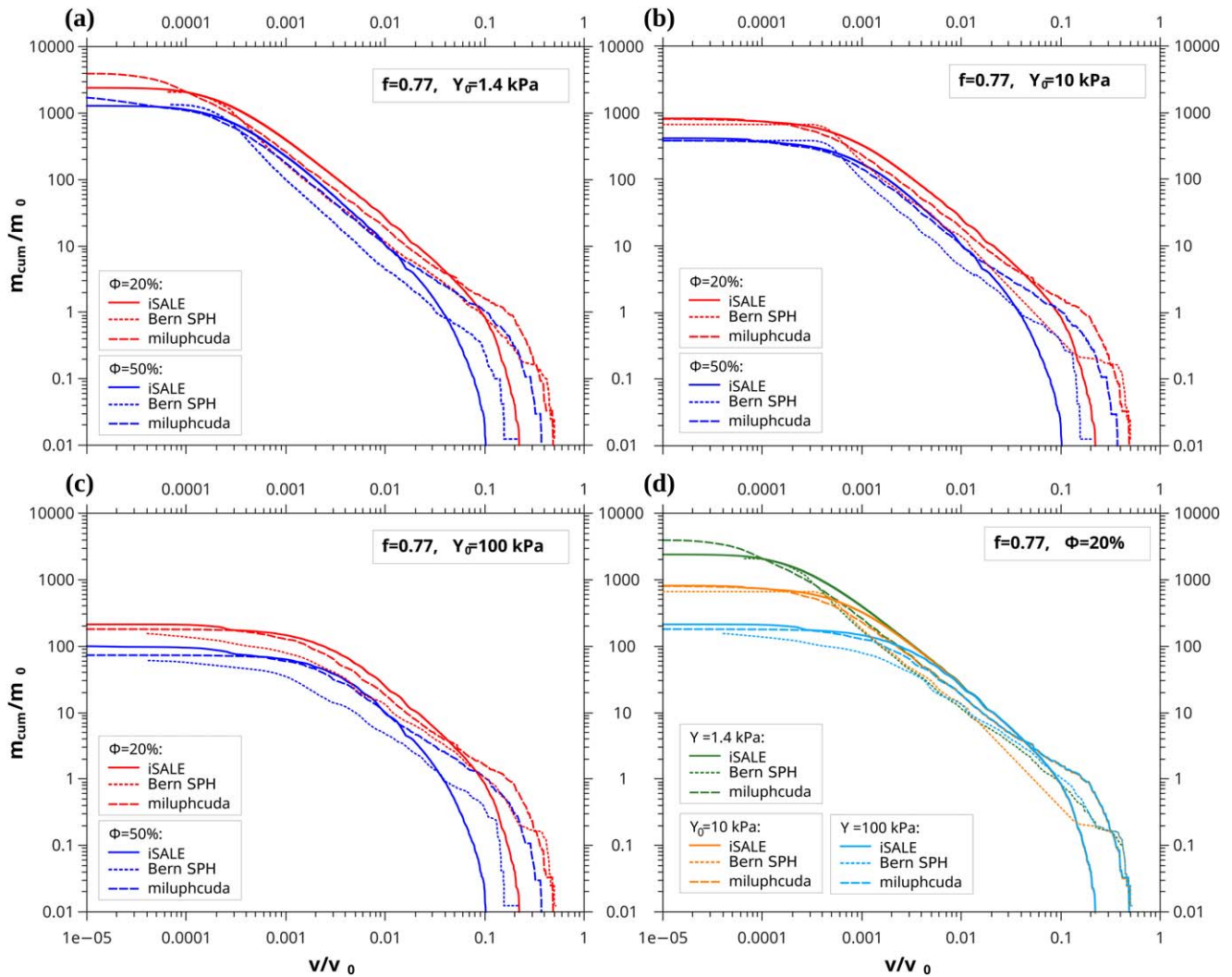


Figure 7. Cumulative ejecta mass over launch velocity for the benchmark scenarios, a DART-like impact into regolith targets, for iSALE (solid lines), Bern SPH (dotted lines), and miluphcuda (dashed lines). Results are plotted for 20% and 50% porosity, as well as all three cohesions in panels (a), (b), and (c). Panel (d) combines all three cohesions for a single porosity of 20%. Colors represent the material porosity (a–c) or cohesion (d). m_0 and v_0 are the impactor mass (600 kg) and velocity (6 km s^{-1}), respectively.

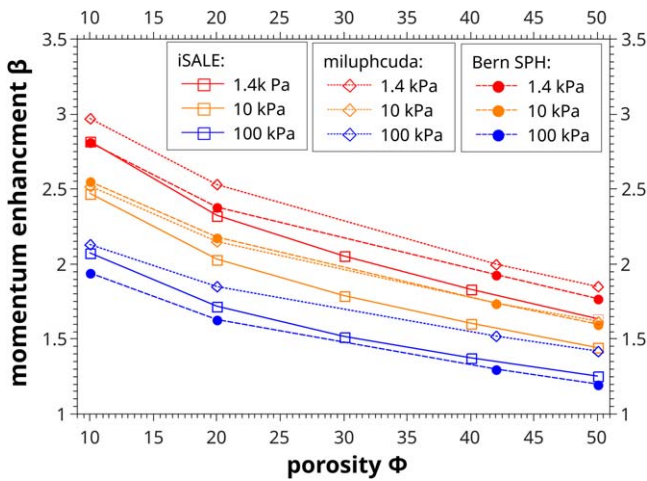


Figure 8. Benchmark results for all three codes in regolith targets for a DART-like impact. Results for iSALE-2D are shown by hollow symbols, and the trend is indicated by solid lines. Results for Bern SPH are shown by filled symbols, and the trend is indicated by dashed lines. Colors represent the material cohesion. The 600 kg impactor has a velocity of 6 km s^{-1} .

relationships. We analyzed the slope of the power-law functions of the cumulative mass plots (Figure 7) by fitting scaling relationships from the literature (Housen & Holsapple 2011), which relate the normalized ejected masses to the normalized ejection velocities as follows:

$$\frac{m_{\text{cum}}}{m_0} = C \left[\frac{v}{v_0} \left(\frac{\rho}{\delta} \right)^{\frac{3\nu-1}{3\mu}} \right]^{-3\mu}, \quad (8)$$

with the material-dependent exponent μ , the scaling factor C , the exponent ν (typically set to 0.3–0.4), the target density ρ , and the projectile density δ . We take into account the data range outside of the plateau of maximum ejected mass, and with speeds slower than the fastest ejecta. The results for the two lower cohesions of 1.4 kPa and 10 kPa, summarized in Table 5 and shown in Figure 9, confirm the agreement between the different codes used for the simulations. Even though the cumulative mass–velocity plots do not exactly overlap, we find a close agreement between the slope of the curves and hence scaling exponent μ . The differences in the results for each code

Table 5
Parameters of Scaling Relationships (Equation (8))

Cohesion Y_0 (kPa)	Porosity Φ (%)	μ		
		iSALE	Bern SPH	miluphcuda
1.4	10	0.40	0.38	0.37
	20	0.41	0.39	0.38
	30	0.41	-	-
	40	0.42	0.40	0.41
	50	0.43	0.42	0.41
10.	10	0.41	0.38	0.36
	20	0.42	0.39	0.37
	30	0.43	-	-
	40	0.44	0.41	0.40
	50	0.47	0.42	0.40
100.	10	0.43	0.35	0.37
	20	0.43	0.36	0.37
	30	0.44
	40	0.47	0.36	0.38
	50	0.50	0.38	0.37

from the average values fall into ranges of ± 0.02 to ± 0.04 for the cases with 1.4 kPa and 10 kPa cohesion, which correspond to about $\pm 5\%$ and $\pm 10\%$, respectively (Table 6). Between 30% and 50% porosity, we determine values between ~ 0.38 and 0.47 , which fall into the same range as results for sand ($\Phi = 35 \pm 5\%$: $\mu = 0.41$), glass microspheres ($\Phi = 36\%$: $\mu = 0.45$), and sand/fly ash ($\Phi = 45\%$: $\mu = 0.4$) as described in the literature (Housen & Holsapple 2011 and references therein). The derived values are slightly larger than the value of 0.37 derived in Section 3.5 based on ejection velocities, and are smaller than the value of 0.56 based on the impact velocity dependence of β . While similar results have been found by Jutzi & Michel (2014), Bruck Syal et al. (2016) found a value of $\mu = 0.44$ based on the impact velocity dependence of β for a porosity of 40%. The increase of μ with increasing porosity shown by all three codes follows the trend observed for scaling relationships for ejected material analyzed by Luther et al. (2018) and Raducan et al. (2019), yielding results similar to those of Raducan et al. (2019).

Our derived values of μ are smaller than those found by impact experiments focusing on material ejection (Cintala et al. (1999) for quartz sand with $0.8\text{--}1.9 \text{ km s}^{-1}$ impact velocity: $\mu = 0.5\text{--}0.66$ at $\Phi = 42\%$; Anderson et al. (2007) for fine sand, average $\mu = 0.59$, or Tsujido et al. (2015) at low velocities of 200 m/s for sand: $\mu = 0.52\text{--}0.64$ at $\Phi = 40\%$ for most shots, apart for two with $\mu = \sim 0.44$ and $\mu = \sim 0.72$) and numerical results for ejection data (Luther et al. (2018), μ ranges from $\mu = 0.43\text{--}0.61$ for $\Phi = 0\%\text{--}42\%$, respectively). However, even though the results from Luther et al. (2018) yield a larger μ in the gravity regime, they find results consistent with ours in the transition range between the gravity- and strength-dominated regimes. The regime (strength or gravity) could play a role when comparing results from ejecta velocity scaling from different studies.

Our results are also in agreement with experimental observations for crater growth observed by Yamamoto et al. (2017) for sand targets ($\Phi = 38\%$). Even though Yamamoto et al. (2017) find values of $\mu = 0.41\text{--}0.66$, they also find a decrease of μ with increasing impact velocity, reaching the

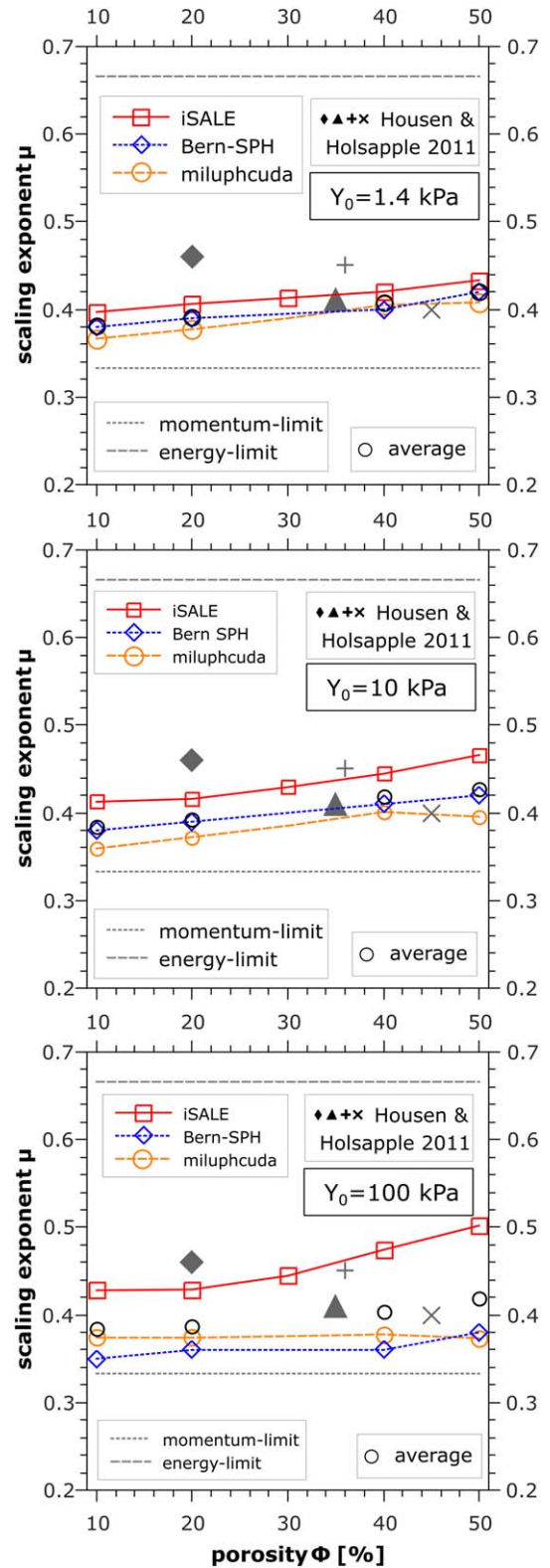


Figure 9. Scaling exponent μ as function of porosity for regolith simulant with a cohesion of 1.4 kPa (top), 10 kPa (middle), and 100 kPa (bottom), and a coefficient of friction of 0.77. The gray symbols denote: diamond—weakly cemented basalt, triangle—sand, plus—glass microspheres, and cross—sand/fly ash as derived by Housen & Holsapple (2011 and references therein). The colors represent the shock physics code. The uncertainty is about the size of the symbols (± 0.01). Only for the 100 kPa cohesion is the uncertainty slightly larger (± 0.02), due to the smaller power-law regime. The black circles show the average values.

Table 6

Average Results from Codes (Table 5) for Scaling Relationships (Equation (7))

Cohesion Y_0 [kPa]	Porosity Φ [%]	Density ρ (kg m^{-3})	Average Result			
			μ	σ_μ	C	σ_C
1.4	10	2430	0.38	0.01	0.151	0.053
	20	2160	0.39	0.01	0.093	0.035
	40	1620	0.41	0.01	0.039	0.021
	50	1350	0.42	0.01	0.026	0.016
10.	10	2430	0.38	0.03	0.151	0.051
	20	2160	0.39	0.02	0.095	0.030
	40	1620	0.42	0.02	0.037	0.015
100.	50	1350	0.43	0.04	0.026	0.018
	10	2430	0.38	0.04	0.108	0.061
	20	2160	0.39	0.04	0.084	0.030
	40	1620	0.40	0.06	0.048	0.024
	50	1350	0.42	0.07	0.036	0.025

lowest values of $\mu = 0.41$ at $\sim 6 \text{ km s}^{-1}$, which agrees with a difference of 0.02 from the averaged results in our benchmark study for the two lower cohesions of 1.4 and 10 kPa (table 6).

For a cohesion of 100 kPa, the slopes of the cumulative mass versus velocity plots from the codes do not align as closely as for smaller cohesions, while the resulting momentum enhancements β for these models are still in close agreement. The resulting scaling parameter μ , when determined from the iSALE results, increases with porosity from 0.43 to 0.5 (0.03 and 0.07 larger than for a cohesion of 10 kPa and 1.4 kPa, respectively), and seems to agree with literature values from Housen & Holsapple (2011) for weakly cemented basalt ($\mu = 0.46$ at $\Phi = 20\%$). The results derived with Bern SPH and miluphcuda are in closer agreement with each other than with those derived with iSALE, and are relatively constant over the shown range of porosity. The deviation from the average result reaches from ± 0.04 to ± 0.07 , which corresponds to about $\pm 10\%$ and $\pm 18\%$, respectively.

This larger deviation in μ for a cohesion of 100 kPa might be caused by the increasing influence of the fastest ejecta upon the total cumulative distribution with decreasing total mass for increasing cohesion (see Figure 7(d)). Bern SPH and miluphcuda generate faster particles than iSALE (Figure 7). However, the larger deviation of the data can also partly be influenced by the choice of the range of data to which the power-law function is fitted. The Bern SPH simulation results use the method described in Raducan et al. (2019), while the iSALE-2D simulation results were derived following the approach from Housen & Holsapple (2011).

Especially in the range of general agreement between the codes, i.e., at cohesions of 1.4 kPa and 10 kPa, the determined averaged scaling parameters (Table 6) can be used to simulate the formation of the DART-induced ejecta curtain based on scaling relationships for longer times or larger domains than in shock physics codes (as done, e.g., by Cheng et al. 2020).

5. Conclusions

In the following, we summarize our results:

1. All three tested shock physics codes, iSALE, Bern SPH, and miluphcuda, can reliably reproduce experimental results from cratering experiments in terms of crater size and momentum enhancement. The resulting crater

diameters for all three codes fall in the range of the experimental scatter, and differ from their average value by $\sim 5\%$ – 20% . For momentum enhancement, differences are much lower, varying only by $\pm 3\%$ with respect to the average values of the codes. The numerical results differ from the experimental results by 1%–10% for the momentum enhancement. These tests can be seen as a successful validation of the material models applied in these codes for impact velocities of a few km s^{-1} .

2. The three codes have been successfully benchmarked against each other. In previous studies, deviations of the resulting momentum enhancement between codes were found to be in the $\pm 10\%$ – 15% range. For the same choice of material models and target parameters, and by aligning the crushing behavior, we improve the agreement between iSALE, miluphcuda, and Bern SPH for momentum enhancement to $\pm 5\%$ from the average value, or better.
3. The setting up of targets for experimental campaigns needs to be done carefully. A slight change of target properties due to variations in the laboratory conditions and target preparation could cause scattering of experimental observations (i.e., crater sizes or the momentum enhancement), due to varied material properties.
4. We have determined ejecta scaling parameters for impacts into regolith for three cohesions between 1.4, 10 and 100 kPa for a range of porosities between 10%–50%, which can be used for scaling analysis in future studies, e.g., to describe and compare the formation of the DART-induced ejecta curtain, which will be observed by LICIAcube. These values are based on cumulative mass distributions versus velocity and are averaged between the codes. While the uncertainty of μ for a cohesion of 100 kPa reaches up to $\pm 20\%$, the values for smaller cohesions down to ~ 1 kPa agree to within $\pm 10\%$.

S.D.R., R.L., M.J., P.M., and Y.Z. appreciate the funding from the European Union’s Horizon 2020 research and innovation program, grant agreement No. 870377 (project NEO-MAPP). C.B. and C.M.S. appreciate support by the German Research Foundation (DFG) project 398488521. P.M. also acknowledges support from CNES and the CNRS through the MITI interdisciplinary programs. TMD and GSC were funded by STFC grant ST/S000615/1. This work was supported by the DART mission, NASA Contract No. 80MSFC20D0004. C.B. and C.M.S. acknowledge support by the High Performance and Cloud Computing Group at the Zentrum für Datenverarbeitung of the University of Tübingen, the state of Baden–Württemberg through bwHPC and the German Research Foundation (DFG) through grant No INST 37/935-1 FUGG. We are thankful for the helpful and constructive reviews from two anonymous reviewers, who helped to improve this manuscript. We gratefully acknowledge the developers of iSALE-2D, including Dirk Elbeshausen, Boris Ivanov, and Jay Melosh. This work used the pySALEPlot software. We also acknowledge the developer of the VIMoD software, Dirk Elbeshausen. iSALE website: <http://www.isale-code.de/>. The SPH code miluphcuda is freely available at <https://github.com/christophmschaefer/miluphcuda>.

Appendix

A.1. Model Parameters

The following tables summarize the input parameters for iSALE (Table A1) and the details of the equations of state (Table A2).

Table A1
Model Parameters for iSALE

General parameters	Regolith simulant
Poisson ratio (basalt)	0.25
Specific heat capacity [J/(kg K)]	1400
Strength parameters	
Lundborg strength:	
Cohesion Y_0 [kPa]	1.4, 10.0, 100.0
Coefficient of friction f	0.77
Maximum strength Y_{\max} [GPa]	1.0 (10.0 ^a)
Thermal softening (Ohnaka)	
Softening constant	1.2
Melt temperate [K]	1900
Simon approximation:	
Simon constant	6·10 ⁹
Simon exponent	3.0
Porosity parameters	See Table 4

Note.

^a 10 GPa was applied in the validation and benchmark at laboratory scale, 1 GPa at DART-scale.

A.2. Strength Weakening

In iSALE, a low-density weakening mechanism is applied, which has been used in previous publications (e.g., Güldemeister et al. 2015; Winkler et al. 2018). The weakening algorithm is applied when the density in a cell falls below the density ρ_{weak} . The threshold density is set to 0.85 times the reference density. The strength is reduced according to

$$Y_{\text{weak}} = Y \cdot \left(\frac{\rho}{\rho_{\text{weak}}}\right)^4 \text{ for } \rho < \rho_{\text{weak}}$$

This low-density weakening is applied when temperatures are below the melt temperature. In addition, we apply a thermal softening model after Ohnaka (1995), using a softening constant of 1.2.

In miluphcuda, we apply a low-density weakening (i.e., below the reference density ρ_0) based on reduction of the cohesion. This in turn affects (reduces) the entire yield strength envelope. For the impact scenarios in this study, $\rho < \rho_0$ usually corresponds to negative pressure states; therefore, this approach reduces strength—both shear and tensile—continuously for decreasing ρ (below ρ_0). The cohesion-reducing factor f_{coh} drops from 1 to 0.5 between ρ_0 and some $\rho_{\text{limit}} < \rho_0$ and from 0.5 to 0 for $0 < \rho < \rho_{\text{limit}}$, where we set ρ_{limit} to 0.85^{*} ρ_0 . In these two regimes, f_{coh} follows power laws with exponent 0.2 for $\rho_{\text{limit}} < \rho < \rho_0$ and exponent 4 for $0 < \rho < \rho_{\text{limit}}$. These parameter choices are based on trials with the validation scenarios, and additionally provide a relatively smooth function f_{coh} , which is numerically advantageous. These parameters are applied to all miluphcuda simulations in this study.

In Bern SPH, we apply a strain-based weakening model. A linear relation between cohesion Y_0 and total strain ε_{tot} is used, and it is assumed that for $\varepsilon_{\text{tot}} \geq 1$ cohesion is lost. The tensile

Table A2

Parameters for the Equations of State Used for the PVC and Regolith Simulant Used by All Three Shock Physics Codes

	PVC (Polyethylene)	Regolith simulant
Reference density [kg m ⁻³]	995.0	2 700.0
Spec. heat capacity [K/kg]	1 000.0	1 000.0
Bulk modulus [GPa]	7.6	26.7
Tillotson B constant [GPa]	0	26.7
Tillotson E0 constant [J kg ⁻¹]	0	4.87 e8
Tillotson a constant	0	0.5
Tillotson b constant	0	1.5
Tillotson alpha constant	0	5.
Tillotson beta constant	0	5.
SIE incipient vaporization [J kg ⁻¹]	4.72D+6	4.72D+6
SIE complete vaporization [J kg ⁻¹]	18.2D+6	18.2D+6

strength is defined by extrapolating the yield strength (versus pressure) curve (Equation (4)) to intersect the pressure axis. Additionally, we limit the maximum negative pressure to $P_{\text{min}} \geq -Y_0$.

ORCID iDs

Robert Luther  <https://orcid.org/0000-0002-0745-1467>
 Sabina D. Raducan  <https://orcid.org/0000-0002-7478-0148>
 Christoph Burger  <https://orcid.org/0000-0001-7120-4260>
 Kai Wünnemann  <https://orcid.org/0000-0001-5423-1566>
 Martin Jutzi  <https://orcid.org/0000-0002-1800-2974>
 Christoph M. Schäfer  <https://orcid.org/0000-0002-0341-3738>
 Detlef Koschny  <https://orcid.org/0000-0001-8690-3507>
 Thomas M. Davison  <https://orcid.org/0000-0001-8790-873X>
 Gareth S. Collins  <https://orcid.org/0000-0002-6087-6149>
 Yun Zhang  <https://orcid.org/0000-0003-4045-9046>
 Patrick Michel  <https://orcid.org/0000-0002-0884-1993>

References

- Amsden, A., Ruppel, H., & Hirt, C. 1980, SALE: A simplified ALE computer program for fluid flow at all speeds, LA-8095, Los Alamos Scientific Lab., <https://doi.org/10.2172/5176006>
- Anderson, J. L. B., Cintala, M. J., Siebenaler, S. A., & Barnouin-Jha, O. S. 2007, *LPSC*, **38**, 2266
- Benz, W., & Asphaug, E. 1994, *Icar*, **107**, 98
- Benz, W., & Asphaug, E. 1995, *CoPhC*, **87**, 253
- Bruck Syal, M., Michael, O. J., & Miller, P. L. 2016, *Icar*, **269**, 50
- Cheng, A. F., Rivkin, A. S., Michel, P., et al. 2018, *P&SS*, **157**, 104
- Cheng, A. F., Stickle, A. M., Fahnestock, E. G., et al. 2020, *Icar*, **352**, 113989
- Chourey, S., Koschny, D., Rott, M., & Schmausser, C. 2020, *P&SS*, **194**, 105112
- Cintala, M. J., Berthoud, L., & Hörz, F. 1999, *M&PS*, **34**, 605
- Collins, G. S., Melosh, H. J., & Ivanov, B. A. 2004, *M&PS*, **39**, 217
- Collins, G. S., Melosh, H. J., & Wünnemann, K. 2011, *IJIE*, **38**, 434
- Davis, R. O., & Selvadurai, A. P. S. 2005, *Plasticity and Geomechanics* (Cambridge: Cambridge Univ. Press), 287
- Davison, T. M., Collins, G. S., & Bland, P. A. 2016, *ApJ*, **821**, 68
- Dotto, E., Della Corte, V., Amoroso, M., et al. 2021, *P&SS*, **199**, 105185
- Durda, D. D., Walker, J. D., Chocron, S., et al. 2019, *P&SS*, **178**, 104694
- Elbeshhausen, D., Wünnemann, K., & Collins, G. S. 2009, *Icar*, **204**, 716
- Grishin, E., Malamud, U., Perets, H. B., Wandel, O., & Schäfer, C. M. 2020, *Natur*, **580**, 463
- Güldemeister, N., Wünnemann, K., Durr, N., & Hiermaier, S. 2013, *M&PS*, **48**, 115

- Güldemeister, N., Wünnemann, K., & Poelchau, M. H. 2015, in *Large Meteorite Impacts and Planetary Evolution V* (Vol. 518) ed. G. R. Osinski & D. A. Kring (Washington, DC: GSA), 17
- Haghighipour, N., Maindl, T. I., Schäfer, C. M., & Wandel, O. J. 2018, *ApJ*, **855**, 60
- Holsapple, K. A., & Housen, K. R. 2012, *Icar*, **221**, 875
- Housen, K. R., & Holsapple, K. A. 2011, *Icar*, **211**, 856
- Housen, K. R., & Holsapple, K. A. 2015, *LPSC*, **46**, 2894
- Ivanov, B. A., Deniem, D., & Neukum, G. 1997, *IJIE*, **20**, 411
- Jutzi, M. 2015, *P&SS*, **107**, 3
- Jutzi, M., Benz, W., & Michel, P. 2008, *Icar*, **198**, 242
- Jutzi, M., Michel, P., Hiraoka, K., Nakamura, A. M., & Benz, W. 2009, *Icar*, **201**, 802
- Jutzi, M., & Michel, P. 2014, *Icar*, **229**, 247
- Jutzi, M., Thomas, N., Benz, W., et al. 2013, *Icar*, **226**, 89
- Kowitz, A., Güldemeister, N., Reimold, W. U., Schmitt, R. T., & Wünnemann, K. 2013, *E&PSL*, **384**, 17
- Lundborg, N. 1968, *Int. J. Rock Mech. Min. Sci.*, **5**, 427
- Luther, R., Artemieva, N., Ivanova, M., Lorenz, C., & Wünnemann, K. 2017, *M&PS*, **52**, 979
- Luther, R., Boustie, M., Hebert, D., et al. 2019, EPSC-DPS Joint Meeting 2019, **14**, 1776
- Luther, R., Zhu, M.-H., Collins, G. S., & Wünnemann, K. 2018, *M&PS*, **53**, 1705
- Melosh, H. J., Ryan, E. V., & Asphaug, E. 1992, *JGR*, **97**, 14735
- Michel, P., Küppers, M., & Campo Bagatin, A. 2022, *PSJ*, **3**, 160
- Nyffeler, B. 2004, PhD thesis, Univ. of Bern
- Ohnaka, Mitiyasu 1995, *GeoRL*, **22**, 25
- Pierazzo, E., Artemieva, N. A., Asphaug, E., et al. 2008, *M&PS*, **43**, 1917
- Prieur, N., Rolf, T., Luther, R., Werner, S., & Wünnemann, K. 2017, *JGRE*, **122**, 1704
- Owen, J. M., DeCoster, M. E., Graninger, D. M., & Raducan, S. D. 2022, *PSJ*, **3**, 218
- Raducan, S. D., Davison, T. M., Luther, R., & Collins, G. S. 2019, *Icar*, **329**, 282
- Raducan, S. D., Davison, T. M., & Collins, G. S. 2020, *P&SS*, **180**, 104756
- Raducan, S. D., & Jutzi, M. 2022, *PSJ*, submitted
- Rivkin, A. S., Chabot, N. L., Stickle, A. M., et al. 2021, *PSJ*, **2**, 173
- Schäfer, C., Riecker, S., Maindl, T. I., et al. 2016, *A&A*, **590**, A19
- Schäfer, C. M., Scherrer, S., Buchwald, R., et al. 2017, *P&SS*, **141**, 35
- Schäfer, C. M., Wandel, O. J., Burger, C., et al. 2020, *A&C*, **33**, 100410
- Schimmerohn, M., Watson, E., Gulde, M., Kortmann, L., & Schäfer, F. 2019, *AcAau*, **156**, 297
- Stephens, D. R., & Lilley, E. M. 1970, *Sci*, **167**, 731
- Stickle, A. M., Bruck Syal, M., Cheng, A. F., et al. 2020, *Icar*, **338**, 113446
- Stickle, A. M., Christoph, B., Wendy, K. C., et al. 2022, *PSJ*, submitted
- Tsujido, S., Arakawa, M., Suzuki, A. I., & Yasui, M. 2015, *Icar*, **262**, 79
- Walker, J. D., Chocron, S., Durda, D. D., et al. 2013, *IJIE*, **56**, 12
- Walker, J. D., & Chocron, S. 2015, *Procedia Engineering*, **103**, 636
- Winkler, R., Luther, R., Poelchau, M. H., Wünnemann, K., & Kenkmann, T. 2018, *M&PS*, **53**, 1733
- Wünnemann, K., Collins, G. S., & Melosh, H. J. 2006, *Icar*, **180**, 514
- Wünnemann, K., Zhu, M.-H., & Stöffler, D. 2016, *M&PS*, **51**, 1762
- Yamamoto, S., Hasegawa, S., Suzuki, A. I., & Matsunaga, T. 2017, *JGRE*, **122**, 1077
- Zhang, Y., Michel, P., Richardson, D. C., et al. 2021, *Icar*, **362**, 114433